J. Fluid Mech. (2006), vol. 569, pp. 465–480. © 2006 Cambridge University Press
doi:10.1017/S0022112006002758 Printed in the United Kingdom

Nonlinear three-dimensional flow in the lid-driven square cavity

By S. ALBENSOEDER AND H. C. KUHLMANN
Vienna University of Technology, 1040 Vienna, Austria

(Received 16 June 2005 and in revised form 17 July 2006)

The three-dimensional flow in a lid-driven cuboid is investigated numerically. The geometry is an extension to three dimensions of the lid-driven square cavity by translating the two-dimensional lid-driven cavity parallel to the third orthogonal direction. The incompressible Navier–Stokes equations are discretized by a pseudospectral Chebyshev-collocation method. The singularities caused by the discontinuous velocity boundary conditions are reduced by including asymptotic analytical solutions in the solution ansatz. The flow is computed for Reynolds numbers above the critical onset of Taylor–Görtler vortices. Nonlinear Taylor–Görtler cells are calculated for periodic and for realistic no-slip endwall conditions. For periodic boundary conditions the bifurcation is either sub- or supercritical, depending on the wavenumber. The limiting tricritical case arises near the critical wavenumber of the linear-stability problem. On the other hand, no-slip endwall conditions have a significant effect on the supercritical three-dimensional flow. In agreement with recent experimental results we find that Taylor–Görtler vortices are suppressed near no-slip endwalls.

1. Introduction

The flow in a square cavity, driven by the steady tangential motion of a lid, is a classical problem in fluid mechanics. The simple geometry makes this setup ideal to study the behaviour of vortices in closed domains. Moreover, the lid-driven cavity is one of the most popular numerical benchmarks.

To date most studies of the lid-driven cavity have been devoted to incompressible Newtonian flows. In an infinitely extended cavity the small-Reynolds-number flow is two-dimensional. In addition to a single primary vortex (Burggraf 1966) an infinite sequence of counter-rotating viscous corner eddies exist in the two wedges formed by the stationary rigid walls (Moffatt 1964; Pan & Acrivos 1967). When the Reynolds number Re increases, the corner eddies grow larger and, for $Re \gtrsim 10^3$, a third eddy separates from the stationary wall near the upstream corner of the moving lid (Schreiber & Keller 1983).

It has been shown by Koseff *et al.* (1983) that the flow becomes three-dimensional at sufficiently high Reynolds numbers. The resulting flow structures have been termed Taylor–Görtler-like vortices (for an experimental visualization, see Rhee, Koseff & Street 1984), because of similarities of the local basic two-dimensional flow and the resulting three-dimensional patterns with the respective flows in the Taylor and Görtler problems (see e.g. Drazin & Reid 1981).

Most past investigations have been carried out for Reynolds numbers much larger than the critical value for the onset of Taylor–Görtler vortices and for span lengths which were one or three times the cavity height. Under these conditions the

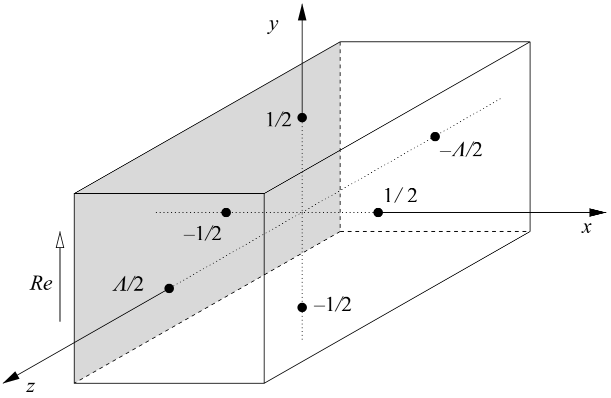

FIGURE 1. Geometry of the lid-driven cavity. The moving wall is shaded in grey.

Taylor–Görtler vortices are either time-dependent (Deville, Lê & Morchoisne 1992) or strongly influenced by the finite span length, or both. Since a three-dimensional Bödewadt-type of flow is induced by radial pressure gradients in the vicinity of no-slip endwalls (de Vahl Davis & Mallinson 1976; Koseff & Street 1984*a*; Chiang, Hwang & Sheu 1997), the precise onset of the three-dimensional flow, the dependence on the governing parameters, and the physical mechanisms of instability remained poorly understood (Triantafillopoulos & Aidun 1990). These and other results on the lid-driven cavity-flow problem have been summarized by Shankar & Deshpande (2000).

More recently, linear-stability analyses have been carried out in order to understand the onset of Taylor–Görtler vortices. In this regard, numerical calculations for an infinitely extended system, unperturbed by endwall effects, have played a major role. While the neutral Reynolds number for the onset of time-dependent two-dimensional flows is rather high (Goodrich, Gustafson & Halasi 1990; Poliashenko & Aidun 1995) the critical Reynolds number for the onset of three-dimensional Taylor–Görtler vortices is only $Re \approx 785$. The critical threshold has been calculated independently by Theofilis (2000) and Albensoeder, Kuhlmann & Rath (2001) (see also Ding & Kawahara 1998, 1999; Spasov *et al.* 2003; Shatrov, Mutschke & Gerbeth 2003). The numerical three-dimensional linear stability analysis of Albensoeder *et al.* (2001) covers a wide range of cross-sectional aspect ratios, analyses the qualitatively different critical modes, and explains the centrifugal mechanism in terms of energy budgets and the criterion proposed by Sipp & Jacquin (2000).

Our present investigation is concerned with finite-amplitude cavity flows at moderately supercritical Reynolds numbers. In § 2 the problem is formulated mathematically, the numerical method is introduced, and the code is validated. The results of the numerical simulations are presented in § 3. Finally, the results are summarized in the Conclusions.

2. Methods of investigation

2.1. *Problem formulation*

We consider the incompressible flow of a Newtonian fluid of density ρ and kinematic viscosity ν in a square cavity of width and height d, and depth L. The flow is driven by the tangential motion in the y-direction of the lid located at $x = -d/2$ (figure 1). Using the scales d, ν/d, d^2/ν, and $\rho\nu^2/d^2$ for length, velocity, time, and pressure, respectively, the fluid motion is governed by the Navier–Stokes and continuity equations

$$\frac{\partial \boldsymbol{u}}{\partial t} + \boldsymbol{u}\cdot\nabla\boldsymbol{u} = -\nabla p + \Delta\boldsymbol{u}, \tag{2.1a}$$

$$\nabla\cdot\boldsymbol{u} = 0, \tag{2.1b}$$

which must be solved in the non-dimensional domain $(x, y, z) \in [-1/2, 1/2]^2 \times [-\Lambda/2, \Lambda/2]$, where $\Lambda = L/d$ is the span aspect ratio.

On the three stationary sidewalls the velocity field $\boldsymbol{u} = (u, v, w)$ must satisfy the no-slip and no-penetration boundary conditions

$$\boldsymbol{u}(y = \pm 1/2) = \boldsymbol{u}(x = 1/2) = 0. \tag{2.2}$$

The no-slip condition on the wall moving with velocity V requires

$$\boldsymbol{u}(x = -1/2) = Re\,\boldsymbol{e}_y, \qquad \text{where} \qquad Re = \frac{Vd}{\nu} \tag{2.3}$$

is the Reynolds number.

In the z-direction two sets of boundary conditions will be used. The real, experimental flow conditions must be modelled by rigid boundary conditions

$$\boldsymbol{u}(z = \pm\Lambda/2) = 0. \tag{2.4}$$

On the other hand, the periodic boundary conditions

$$\boldsymbol{u}(z = \Lambda/2) = \boldsymbol{u}(z = -\Lambda/2) \quad \text{and} \quad p(z = \Lambda/2) = p(z = -\Lambda/2) \tag{2.5}$$

allow the investigation of two- and three-dimensional flows unperturbed by the endwalls, except for enforcing the periodicity. These boundary conditions should adequately model the flow in the central region of an extended system when $\Lambda \gg 1$.

2.2. *Numerical methods*

The problem is solved by three-dimensional simulation using an extension of the two-dimensional method of Botella & Peyret (1998) and Botella (1998) in which the flow is calculated in primitive variables. The spatial discretization in the (x, y)-plane is based on $\mathscr{P}_N$–$\mathscr{P}_{N-2}$ Chebyshev collocation (Peyret 2002) on a $N_x \times N_y$ Gauss–Lobatto grid. The interpolation polynomials are of order N for the velocities and of order $N - 2$ for the pressure. Owing to this ansatz, boundary conditions for the pressure need not be specified. For the discretization in the z-direction we have to distinguish between rigid and periodic boundary conditions. For rigid boundary conditions the same discretization is used as for the x- and y-directions. For periodic boundary conditions we employ the Fourier modes

$$f(z) = \sum_{n=-(N_z-1)/2}^{(N_z-1)/2-1} a_n \mathrm{e}^{\mathrm{i}n\pi z} \tag{2.6}$$

of the Fourier space $\mathscr{F}_{N-2}$ on an equidistant grid. Using this ansatz the boundary conditions at the endwalls can be changed easily from rigid to periodic, and vice versa, by replacing the respective derivative matrices.

The time integration is accomplished by an Adams–Bashforth Euler-backward method which is second order in time for the velocity components and the pressure (Botella & Peyret 1998; Heinrichs 1998). The Darcy problem arising in the projection step is solved by the Uzawa method. The leading equations are of Helmholtz-type and they are solved by a direct Helmholtz solver (Haidvogel & Zang 1979; Haldenwang *et al.* 1984).

In the lid-driven-cavity problem the boundary conditions are singular at the corners made by the moving and the steady walls. To improve the accuracy, the asymptotic solutions for vanishing distance from the edge of the respective two-dimensional edge problems (Hancock, Lewis & Moffatt 1981; Gupta, Manohar & Noble 1981) are incorporated into the ansatz. This reduces the order of the singularities at the two edges $(x, y, z) = (-1/2, \pm 1/2, z)$ for the remaining numerical problem. The asymptotic solutions are considered up to second order. The first-order asymptotic solutions are the solutions of the Stokes-flow edge problems. The second-order term takes into account nonlinear inertia corrections to the creeping-flow approximation. Hence, the full solution $(\boldsymbol{u}, p)$ is written as a sum of the two-dimensional asymptotic solutions for both edges $[\boldsymbol{u}_{c,i}(x, y), p_{c,i}(x, y)]$ and the deviation $(\boldsymbol{u}_*, p_*)$ from the full solution:

$$\boldsymbol{u} = \sum_{i=1}^{2} \boldsymbol{u}_{c,i} + \boldsymbol{u}_*, \qquad p = \sum_{i=1}^{2} p_{c,i} + p_*. \tag{2.7}$$

Numerically, we solve for $\boldsymbol{u}_*$ and p_* instead of $\boldsymbol{u}$ and p. For periodic boundary conditions the order of all singularities is reduced by this approach. For rigid boundary conditions in the z-direction not all singularities can be reduced: the discontinuity of the tangential velocities along the edges between the endwalls and the moving wall prevail. Yet, the accuracy of the numerical solution in the bulk of the cavity is improved by the ansatz (2.7). A detailed description of the numerical method and its convergence for rigid and periodic boundary conditions is given in Albensoeder & Kuhlmann (2005) and Albensoeder (2004).

In order to compare the results of the numerical simulation with accurate stability analyses, the linear-stability methods employed in Albensoeder *et al.* (2001) were re-coded using the same collocation method and the subtraction of the corner singularities as for the three-dimensional simulation. The re-formulation is required for a consistent comparison between linear and nonlinear results. The stability analysis is very useful for an accurate determination of the type of bifurcation if the bifurcation is only weakly sub- or supercritical. Moreover, the stability analysis based on the present collocation method allows an independent comparison with the linear-stability results of Albensoeder *et al.* (2001).

2.3. *Validation of the numerical simulation*

To validate the numerical-simulation code comparisons are made with existing data for steady and time-dependent flows. For comparisons of steady states, the computed flow was considered converged to the true steady state after the rates of change of the velocity components have become sufficiently small, satisfying the criterion

$$\frac{\max_{\boldsymbol{x},i} |u_i(\boldsymbol{x}, t) - u_i(\boldsymbol{x}, t - \Delta t)|}{\Delta t |Re|} \leqslant \epsilon_s, \qquad \text{with} \quad \epsilon_s = 10^{-7}. \tag{2.8}$$

For all test cases considered, the flow for sufficiently large times was found to be independent of the initial conditions.

One of the standard benchmarks is the steady two-dimensional flow for $Re = 1000$. We find the velocity fields of the converged flow state to be identical up to the last significant decimal figures of the data tabulated by Botella & Peyret (1998) and Botella (1998) (see also Albensoeder & Kuhlmann 2005).

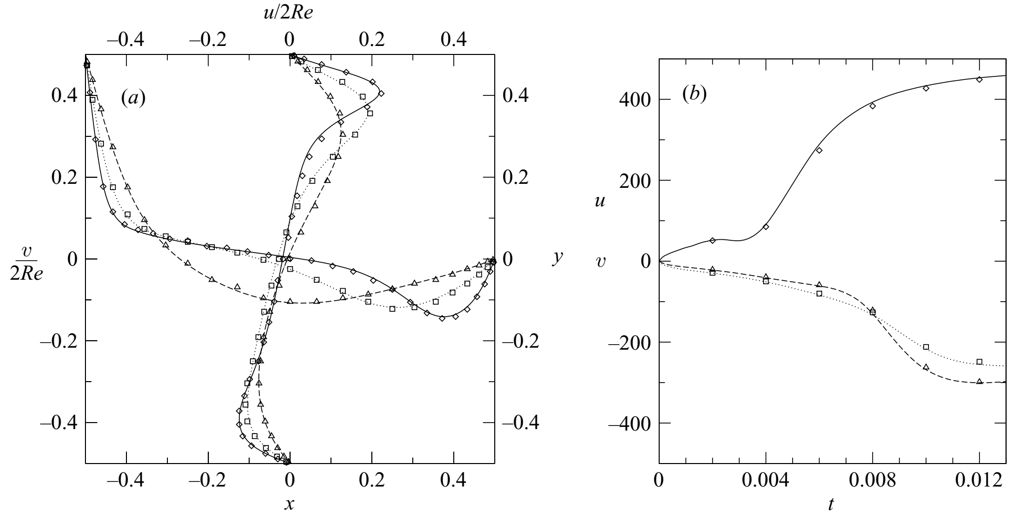

FIGURE 2. (*a*) Normal velocities on the centrelines $(x, 0, 0)$ and $(0, y, 0)$ in the cubic cavity for $\Lambda = 1$ using a resolution $N_x \times N_y \times N_z = 32 \times 32 \times 24$. The Reynolds numbers are $Re = 100$ (dashed line), $Re = 400$ (dotted line), and $Re = 1000$ (solid line). The symbols △ ($Re = 100$), □ ($Re = 400$), and ◇ ($Re = 1000$) represent the results of Ku *et al.* (1987), extracted from their figures. (*b*) Velocities $u(\boldsymbol{x}_1)$ (solid line, ◇), $u(\boldsymbol{x}_2)$ (dotted line, □), and $v(\boldsymbol{x}_3)$ (dashed line, △) as functions of time t for $Re = 1000$, and $\Lambda = 2$. The velocities are monitored at $\boldsymbol{x}_1 = (0, 0.40908, 0)$, $\boldsymbol{x}_2 = (0, -0.27777, 0)$, and $\boldsymbol{x}_3 = (0, -0.29797, 0)$. The resolution is $N_x \times N_y \times N_z = 32 \times 32 \times 32$. Symbols indicate the results of Guermond *et al.* (2002).

As a second test case, the three-dimensional flow in a cubical cavity ($\Lambda = 1$) is considered. In figure 2(*a*) the velocity profiles of u and v on the centrelines $(0, y, 0)$ and $(x, 0, 0)$ are displayed in comparison to the results of Ku *et al.* (1987) for $Re = 100$, $Re = 400$ and $Re = 1000$. As can be seen in figure 2(*a*) the present calculations (lines) are in very good agreement with the results of Ku *et al.* (1987) (symbols).

Finally, a comparison is made for a three-dimensional transient flow in a cavity whose lid was suddenly set into motion with $Re = 10^3$. This case has been studied by Guermond *et al.* (2002) for an aspect ratio $\Lambda = 2$. In figure 2(*b*) three velocities are monitored as functions of time. The monitoring locations are chosen near the location of the extremal velocities on the centrelines (see figure 2*a*). Again the correlation between the present results and those of Guermond *et al.* (2002) is very good. Further comparisons and validation data are given in Albensoeder & Kuhlmann (2005) and Albensoeder (2004).

2.4. *Validation of the linear-stability analysis*

The linear-stability problem for the steady two-dimensional flow was solved in Albensoeder *et al.* (2001). It was shown that four different instability branches exist, depending on the cross-sectional aspect ratio Γ. For all branches the instability is due to centrifugal effects.

The most dangerous three-dimensional perturbation $(\tilde{\boldsymbol{u}}, \tilde{p})$ of the basic two-dimensional flow $(\boldsymbol{u}_0, p_0)$ takes the form of a normal mode $(\tilde{\boldsymbol{u}}, \tilde{p}) = (\hat{\boldsymbol{u}}, \hat{p})(x, y) \times \exp[\sigma t + \mathrm{i}(k_c z - \Omega_c t)]$ which is a wave characterized by the wavenumber k_c in the z-direction. For the square cavity, the critical oscillation frequency vanishes: $\Omega_c = 0$.

The results for the square cavity obtained in Albensoeder *et al.* (2001) have been confirmed independently by Spasov *et al.* (2003) and by Shatrov *et al.* (2003), and

	Re_c	k_c	Ω_c	$N_x \times N_y$	$N_x \times N_y$ (error estimate)
Present	783.9 ± 0.4	15.446 ± 0.003	0.0	34×34	42×42
Albensoeder *et al.* (2001)	786 ± 6	15.43 ± 0.06	0.0	141×141	71×71
Shatrov *et al.* (2003)	784.22	15.450 ± 0.005	0.0	71×71	–
Spasov *et al.* (2003)	785	15.40	0.0	141×141	–
Theofilis (2000)	782	15.4	0.0	48×48	–
Theofilis *et al.* (2004)	782.61	15.37	0.0	48×48	–

Table 1. Comparison of the critical parameters to results from Albensoeder *et al.* (2001) and other authors. The error is estimated by comparison with the critical data obtained by calculations with a lower resolution given in the last column.

they are in agreement with the values for the square cavity of Theofilis, Duck & Owen (2004). Our previous linear-stability results also agree nicely with the critical data of the present linear-stability analysis which is based on collocation. A quantitative comparison is provided in table 1. Further confidence is gained from the coincidence of the critical data with the corresponding results of the full three-dimensional simulations. It should be mentioned, however, that the critical data obtained by both of our independent linear-stability analyses as well as by our numerical simulations differ significantly from the critical data reported by Theofilis *et al.* (2004) when the cross-section is not a square ($\Gamma \neq 1$).

3. Results

The critical three-dimensional flow in the square cavity consists of steady Taylor–Görtler vortices (Albensoeder *et al.* 2001). Slightly above the threshold the spectrum of excited Fourier modes in the z-direction is confined to a narrow band around the critical wavenumber k_c (see e.g. Newell & Whitehead 1969). Hence, we are primarily interested in spatial periods Λ comparable to the critical wavelength $\lambda_c = 2\pi/k_c$.

When the Reynolds number is increased quasi-statically past its critical value the slightly supercritical flow for $\lambda_c = 2\pi/k_c$ remains stationary. The spectrum of the flow is obtained from the simulation data by discrete Fourier transform. For example, the complex amplitudes $a_{w,m}(x, y)$ of the transverse velocity field $w(x, y, z, t)$ are

$$a_{w,m}(x, y) = \frac{1}{N_z - 1} \sum_{i=1}^{N_z-1} w(x, y, z_i) \mathrm{e}^{2\pi \mathrm{i} m(i-1)/(N_z-1)}. \tag{3.1}$$

The wavenumber of the mth Fourier mode is $k = m\, k_0$, where $k_0 = 2\pi/\Lambda$, and the modulus $A_{w,m}$ of each Fourier mode of w is given by

$$A_{w,m} = |a_{w,m}|. \tag{3.2}$$

In the following, the three-dimensional time-dependent problem (2.1)–(2.2) is solved using the periodic boundary conditions (2.5).

3.1. *Bifurcation for $k_0 = k_c$*

In a first step, the span aspect ratio is fixed to the critical wavelength $\Lambda = \lambda_c = 2\pi/k_c = 0.407$, i.e. $k_0 = k_c$. Figure 3(*a*) shows the fundamental ($m = 1$) amplitude of the y-component of the steady-state velocity $A_{v,m=1}$ (solid line, □) at the

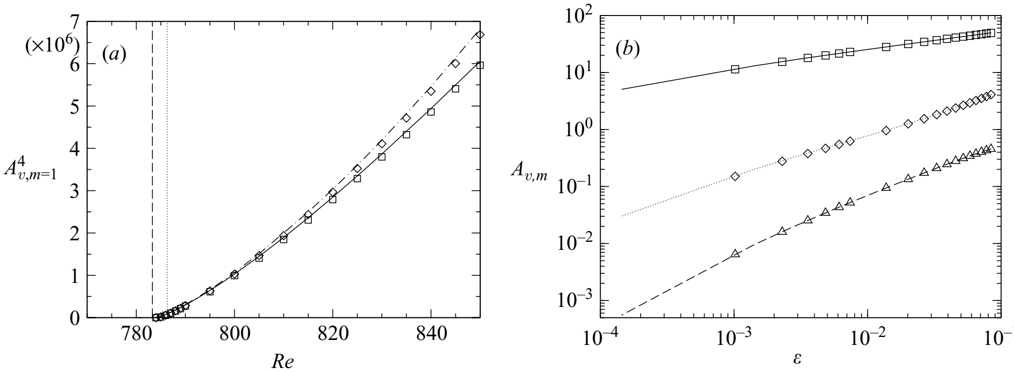

FIGURE 3. (*a*) Fourth power of the amplitude $A_{v,m=1}(x_0, y_0)$ (solid line, □) and of $\max_{x,y} A_{v,m=1}(x, y)$ (dash-dotted line, ◇) as functions of the Reynolds number *Re*. The dashed line marks the results of the linear stability analysis. The dotted line shows the results of Albensoeder *et al.* (2001). (*b*) Amplitudes $A_{v,m}(x_0, y_0)$ with $m = 1$ (solid line, □), $m = 2$ (dotted line, ◇) and $m = 3$ (dashed line, △) as functions of $\varepsilon = (Re - Re_c)/Re_c$. In both plots $\Lambda = 2\pi/k_c = 0.407$. The amplitudes are evaluated at $(x_0, y_0) = (0.263, -0.337)$ using $N_x \times N_y \times N_z = 34 \times 34 \times 25$ grid points (lines). The resolution of the convergence-test calculations (symbols) is $N_x \times N_y \times N_z = 42 \times 42 \times 25$.

monitoring point $(x_0, y_0) = (0.263, -0.337)$ as well as its maximum in the (x, y)-plane, $\max_{x,y} A_{v,m=1}(x, y)$ (dash-dotted line, ◇) as functions of the Reynolds number. Symbols indicate data which were computed with a higher resolution. The good agreement between the results obtained for different resolutions indicates grid convergence of each calculation.

Both curves in figure 3(*a*) indicate a supercritical bifurcation. The present results can be compared with the stationary solutions of the amplitude equation in the absence of spatial variations (see e.g. Cross & Hohenberg 1993)

$$\frac{\mathrm{d}A}{\mathrm{d}t} = \varepsilon A + c_2 |A|^2 A + c_4 |A|^4 A + \cdots \tag{3.3}$$

where

$$\varepsilon = \frac{Re - Re_c}{Re_c}. \tag{3.4}$$

Thus the amplitude should bifurcate either as a square root ($c_2 \neq 0$) or as the fourth root of ε ($c_2 = 0$). However, the amplitude at the monitoring point $(x_0, y_0) = (0.263, -0.337)$ (solid line) does not seem to behave as expected.

To quantify the Reynolds-number dependence of $A_{v,m}(\varepsilon)$ a log-log plot is provided in figure 3(*b*) for the first three harmonics $m \in 1, 2, 3$. The curves are nearly linear. By a regression

$$A_{v,m} = A^{(0)}_{v,m} \varepsilon^{\alpha_m} \tag{3.5}$$

we find an exponent $\alpha_1 = 0.345 \pm 0.019 \approx 1/3$ for the fundamental Fourier mode $m = 1$ (see also table 2). The error was estimated from the coefficients obtained for low and high grid resolutions. The exponents of the first three harmonics can be approximated by $\alpha_m \approx 1/3 + 0.3(m - 1)$ with $m = 1, 2, 3$.

Since the maximum amplitude $\max_{x,y} A_{v,m=1}(x, y)$ (dash-dotted line in figure 3*a*) shows a similar dependence on *Re* as the amplitude at the fixed location, the unexpected scaling cannot be due to a spatial variation of the maximum of the

m	α_m	$A^{(0)}_{v,m}$
1	0.345 ± 0.019	121.7 ± 9.7
2	0.747 ± 0.008	24.32 ± 0.52
3	1.020 ± 0.072	7.0 ± 1.9

TABLE 2. Approximation of the amplitude by $A_{v,m} = A^{(0)}_{v,m} \varepsilon^{\alpha_m}$ for $\Lambda = 2\pi/k_c = 0.407$. The coefficients were calculated by regression of the data from figure 3(*b*). The errors were estimated by comparing resolution of $N_x \times N_y \times N_z = 34 \times 34 \times 25$ and $N_x \times N_y \times N_z = 42 \times 42 \times 25$.

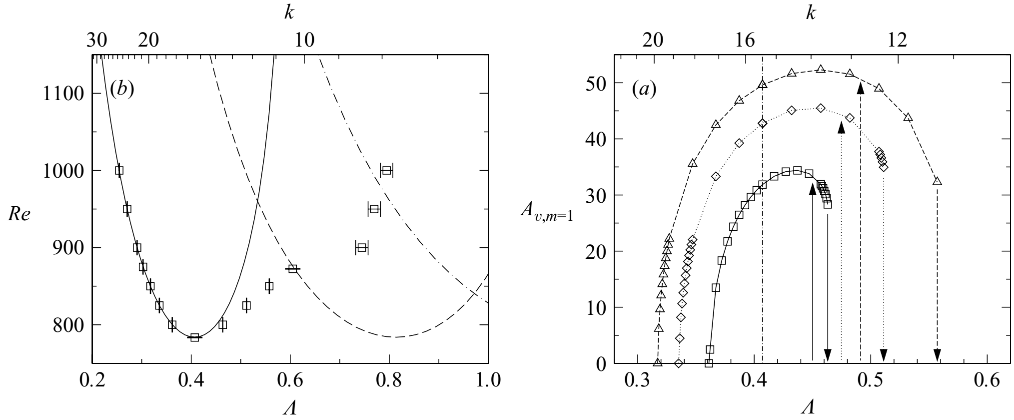

FIGURE 4. (*a*) Neutral curve of the linear stability analysis (solid line) and the nonlinear existence boundary of Taylor–Görtler-vortex pairs (□) as functions of the span aspect ratio Λ and the wavenumber $k = 2\pi/\Lambda$, respectively. The error bars show the stepsize of the quasi-static parameter variation. The dashed and dashed-dotted lines marks the neutral curve with two and three Taylor–Görtler-vortex pairs. (*b*) Amplitude $A_{v,m=1}(x_0, y_0)$ as a function of the span aspect ratio Λ and the wavenumber $k = 2\pi/\Lambda$ for $Re = 800$ (□), $Re = 825$ (◇) and $Re = 850$ (△). Arrows indicate the loci where solution jumps were detected. The amplitude is evaluated at $(x_0, y_0) = (0.263, -0.337)$. The dash-dot line marks the critical wavelength λ_c and the critical wavenumber k_c. The resolution is $N_x \times N_y \times N_z = 34 \times 34 \times 25$ for both plots.

amplitude with ε. Within the investigated range of $\varepsilon \in [0; 0.1]$ the (x, y)-location of the maximum amplitude varies only by $(\Delta x, \Delta y) \approx (0.045, 0.015)$.

3.2. *Variation of the span aspect ratio* Λ

For an exploration of the nonlinear behaviour the span aspect ratio Λ was varied. In order to ensure that the time-asymptotic solution is obtained when computing steady flows the calculation for each parameter set was continued until (2.8) was satisfied. In cases in which the time-asymptotic flow is oscillatory the integration was terminated after a periodic state was reached. For strongly supercritical flows the integration time was at least $T = 0.5$ for each parameter set. For near-critical conditions, the computation time was increased up to $T = O(50)$.

The results of the calculations are shown in figure 4(*a*) where the amplitude $A_{v,m=1}(\Lambda)$ is displayed for the slightly overcritical Reynolds numbers $Re = 800$, 825, and 850. As can be seen, the bifurcation to Taylor–Görtler vortices changes its type: for $\Lambda \lesssim \lambda_c$ the bifurcation is supercritical, whereas it is subcritical for $\Lambda \gtrsim \lambda_c$. The corresponding hysteresis is indicated by arrows in figure 4(*b*). Owing to the transition from a super- to a subcritical bifurcation near $\Lambda = 2\pi/k_c$ quintic terms in the amplitude equation (3.3) must be taken into account. Hence, the steady-state solution must satisfy

$$\varepsilon = c_2 A_{v,m=1}^2 + c_4 A_{v,m=1}^4 \tag{3.6}$$

or, for the positive branch of the bifurcation,

$$A_{v,m=1} = \sqrt{\frac{c_2}{2c_4}} \sqrt{-1 \pm \sqrt{1 + \frac{4c_4}{c_2^2}\varepsilon}}. \tag{3.7}$$

Nonlinear regression yields the coefficients $c_2 = 9.759 \times 10^{-6}$ and $c_4 = 1.015 \times 10^{-8}$. Since the bifurcation at $k = k_c$ is supercritical ($c_2 > 0$) the sign of the inner square root must be positive. A Taylor expansion of (3.7) for $\varepsilon \to 0$ shows that the bifurcating amplitude can be approximated by

$$A_{v,m=1} = \sqrt{\varepsilon / c_2} \tag{3.8}$$

when $\varepsilon \ll c_2^2/4c_4 \approx 1/400$. On the other hand, the amplitude grows like $\sim\varepsilon^{1/4}$ for $\varepsilon \gtrsim O(0.1)$, i.e. for $1 \ll (4c_4\varepsilon/c_2^2)^{1/2}$. Owing to the magnitudes of the coefficients c_2 and c_4 the square-root behaviour of the bifurcation is not visible on the scale $\varepsilon \in [0; 0.1]$ for which the calculations were carried out. Figure 3 shows the intermediate range between the asymptotic limit $A_{v,m=1}(\varepsilon \to 0) \propto \varepsilon^{1/2}$ and $A_{v,m=1}(\varepsilon \gg 1) \propto \varepsilon^{1/4}$. The average exponent of $A_{v,m=1}$ on this intermediate ε-scale is $\alpha_1 = 0.345$. Because of the critical slowing down, calculations for smaller values of ε could not be carried out within a reasonable time.

3.3. *Nonlinear stability boundaries*

The loci $\Lambda_*(Re)$ at which the three-dimensional flow becomes the two-dimensional basic flow are shown in figure 4(*a*) in the (Λ, Re)-plane or, equivalently, the (k, Re)-plane with $k = 2\pi/\Lambda$. The neutral stability boundaries are also shown. For $\Lambda \lesssim \lambda_c$ the nonlinear stability limit Λ_* coincides with the neutral Reynolds number within the error bounds and the transition is continuous. The bifurcation is supercritical ($c_2 > 0$) for the corresponding wavelengths. In contrast, the bifurcation is subcritical ($c_2 < 0$) for $\Lambda \gtrsim \lambda_c$, i.e. the coefficient c_2 changes sign near $\Lambda \approx \lambda_c$. Hence, the Taylor–Görtler vortices break down discontinuously and a tricritical bifurcation point ($c_2 = 0$) must exist for a wavelength slightly larger than λ_c.

When the Reynolds number is sufficiently large the span aspect ratio Λ_* at which the three-dimensional Taylor–Görtler vortices break down to the two-dimensional flow for $\lambda > \lambda_c$ meets the linear stability boundary for the flow with two pairs of Taylor–Görtler vortices (dashed line in figure 4*a*) at $\Lambda \approx 0.6$ between $Re = 873$ and $Re = 900$. For $Re = 850$ the single Taylor–Görtler vortex pair breaks down at $\Lambda = 0.558 \pm 0.001$ (△ in figure 5) and two pairs of Taylor–Görtler bifurcate supercritically (dashed line in figure 4*a*) upon an increase of Λ. However, for $Re \gtrsim 900$ the nonlinear flow of one pair of Taylor–Görtler vortices transforms smoothly, upon an increase of the span aspect ratio, into a flow consisting of two pairs of Taylor–Görtler vortices. This is shown in figure 5 in which the Fourier modes $m = 1$ and $m = 2$ are displayed as functions of Λ. For $Re = 1000$ the amplitude of the second harmonic $m = 2$ grows larger than the amplitude of the fundamental mode $m = 1$ (□ in figure 5) when $\Lambda \gtrsim 0.62$. While the fundamental mode disappears at $\Lambda_* = 0.795 \pm 0.013$, beyond the linear stability boundary for two pairs of Taylor–Görtler vortices, the amplitude of the second harmonic $m = 2$ continues to grow with Λ. The three rightmost Λ_*-points in figure 4(*a*) thus do not mark the collapse of the three-dimensional flow to the basic

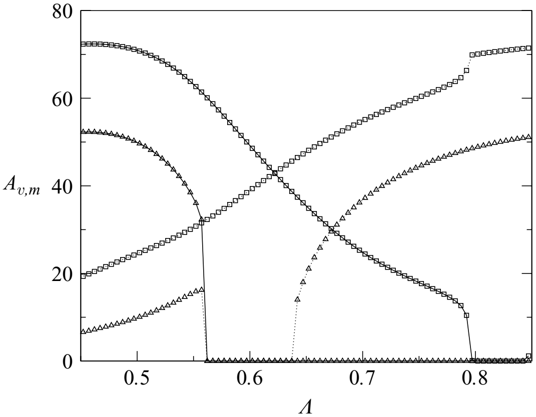

FIGURE 5. Amplitudes $A_{v,m=1}$ (solid line) and $A_{v,m=2}$ (dotted line) as functions of the span aspect ratio Λ for a quasi-static variation of Λ. Symbols denote the Reynolds numbers, $Re=850$ (△) and $Re=1000$ (□). The amplitudes are evaluated at $(x_0, y_0)=(0.263, -0.337)$ and the resolution is $N_x \times N_y \times N_z = 34 \times 34 \times 25$.

two-dimensional flow, but rather the disappearance of the fundamental mode $m=1$. At these bifurcation points the character of the flow has completely changed to a state with two pairs of Taylor–Görtler vortices.

The neutral curves for a number $n_{TG} \in \{1, 2, 3, 4, \ldots\}$ of Taylor–Görtler vortex pairs have identical minima at equally spaced span aspect ratios $\Lambda = n_{TG}\lambda_c$ (figure 4*a*). Since the neutral curves become flatter as n_{TG} increases, the envelope of all neutral curves approaches the line $Re = Re_c$ as $\Lambda \to \infty$. We find that the bifurcation upon increasing Re does not depend on the number of Taylor–Görtler vortices when the aspect ratio is an integer multiple of the critical aspect ratio $\Lambda = n_{TG}\lambda_c$, indicating the absence of sideband instabilities for these values of n_{TG}. At a fixed supercritical Reynolds number, however, the modification of the flow upon a variation of Λ depends on n_{TG}, because the relative amount of compression or dilatation in order to create or annihilate, respectively, a pair of vortices depends on n_{TG}.

Figure 6 shows the loci Λ_* at which the fundamental harmonic of the flow state consisting of one (□), two (◇), three (△), and four (○) Taylor–Görtler vortex pairs vanishes on a quasi-static increase or decrease of Λ, keeping the Reynolds number fixed, or on a quasi-static decrease of Re while keeping the span aspect ratio Λ constant. Which of the two parameters was varied can be seen from the error bars which indicate the step size of the quasi-static variation.

The flows which arise beyond the nonlinear stability boundaries are characterized in figure 7. We first consider two steady Taylor–Görtler vortex pairs. If $Re \geqslant 850$ the Taylor–Görtler vortices lose their stability to a time-dependent state (◇ in figures 6 and 7) when the aspect ratio Λ is increased from $\Lambda = 2\lambda_c$. For $\Lambda < 2\lambda_c$ the transformation from two pairs to a single Taylor–Görtler vortex pair is continuous, as discussed above. Along line *a* in figure 7 the Fourier mode $m=2$ vanishes. The locus is equal to the nonlinear stability boundary of a single Taylor–Görtler vortex pair. Along line *b* the Fourier mode $m=1$ is established upon a decrease of Λ. If $Re < 850$ the flow with two pairs becomes two-dimensional for $\Lambda < \Lambda_*$.

For three Taylor–Görtler vortex pairs (△ in figures 6 and 7) a decrease of Λ results in an oscillating flow state when $Re \geqslant 850$, similar to an increase of Λ for two Taylor–Görtler vortex pairs. We investigated neither the nature of these transitions nor a

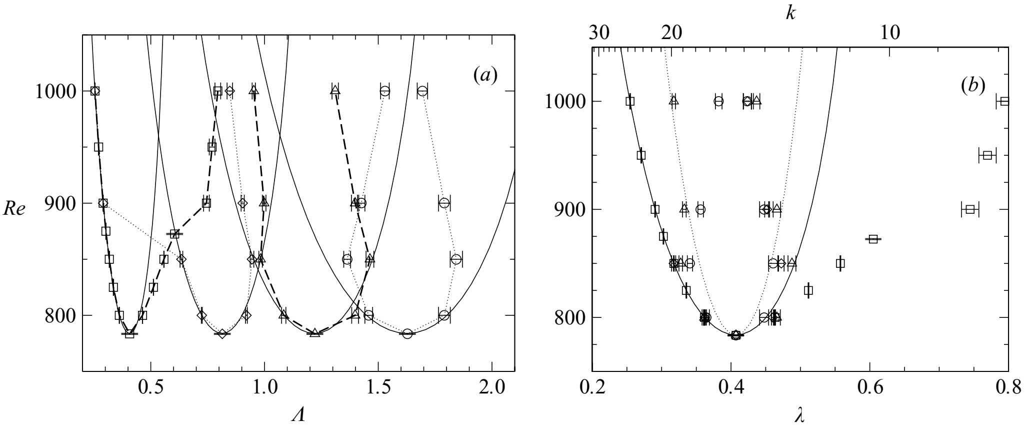

FIGURE 6. Nonlinear stability boundaries of one (□), two (◇), three (△) and four (○) Taylor–Görtler-vortex pairs as functions of the span aspect ratio Λ (*a*) and as functions of the wavelength λ and wavenumber $k = 2\pi/\lambda$ (*b*). Error bars mark the stepsize of the quasi-static variation of the respective parameter. The solid line denotes the curve of neutral stability. The theoretical Eckhaus-stability boundary for $\varepsilon \to 0$ is shown as a dotted line in (*b*). The numerical resolution in the (x, y)-plane was $N_x = N_y = 34$, while the resolution in span direction was $N_z = 25$ for $\Lambda = \lambda_c$ (□), $N_z = 51$ for $\Lambda = 2\lambda_c$ (◇), $N_z = 71$ for $\Lambda = 3\lambda_c$ (△), and $N_z = 95$ for $\Lambda = 4\lambda_c$ (○).

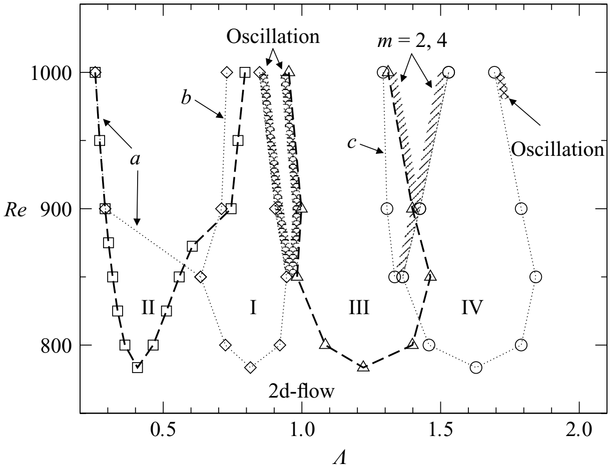

FIGURE 7. Nonlinear stability boundaries of one (□), two (◇), three (△) and four (○) Taylor–Görtler-vortex pairs as functions of the span aspect ratio Λ. All parameters are the same as in figure 6(*a*). The roman numerals indicate the number of Taylor–Görtler-vortex pairs.

possible hysteresis with respect to variations of Λ between both three-dimensional time-dependent states. On increasing Λ for $Re \geqslant 850$, the three steady Taylor–Görtler-vortex pairs are replaced by Taylor–Görtler vortices with $n_{\mathrm{TG}} = 4$. The four-pair flow is spatially modulated with a subharmonic mode $m = 2$. For lower Reynolds numbers the steady Taylor–Görtler vortices again give way to the two-dimensional basic state at Λ_*.

Considering four Taylor–Görtler vortex pairs (○ in figures 6 and 7) we find a transition to a spatially modulated flow upon a decrease of Λ when $Re \geqslant 850$. The dominant Fourier mode in the new flow still is $m = 4$, but also the subharmonic mode $m = 2$ is excited. A further decrease of Λ leads to three Taylor–Görtler vortex pairs ($m = 3$) at the line labelled c in figure 7. At this line the amplitudes of the Fourier modes with $m = 2$ and $m = 4$ vanish. Increasing Λ from $\Lambda = 4\lambda_c$ the steady four-pair flow changes into a five-pair flow. For $Re = 850$ and $Re = 900$ the five-pair flow is found to be steady, whereas it is time-dependent for $Re = 1000$. As before, the three lowermost points in figure 7 indicate the transition to the two-dimensional basic state.

The wavelength $\lambda = \Lambda_* / n_{\mathrm{TG}}$ at which the fundamental Fourier mode of the state with n_{TG} vortex pairs vanishes depends non-monotonical on n_{TG}. From figure 6(a, b) there is a strong tendency that the λ-range of stable Taylor–Görtler vortices shrinks as the number of vortex pairs is increased. In the infinite system ($n_{\mathrm{TG}} \to \infty$) a continuous wavenumber band of Taylor–Görtler vortices is available. The stable range of wave numbers is reduced by the long-wave Eckhaus instability (Eckhaus 1965; Fauve 1998). Near the critical point the reduction amounts to $\varepsilon_{\mathrm{Eckhaus}} = 3\varepsilon_{\mathrm{neutral}}$ (dotted line in figure 6b). For the present finite-length system with $n_{\mathrm{TG}} = 1, 2, 3, 4$ the Eckhaus stability boundary is not obtained for small ε and the stable range of Taylor–Görtler vortices extends close to the neutral curve. Apparently, there is no nearby wavelength in the short system available to be amplified. For larger values of ε, however, the result for the largest system investigated ($n_{\mathrm{TG}} = 4$) may approximate the Eckhaus instability boundary, which is usually much narrower in the strongly nonlinear regime than the band extrapolated from the slightly nonlinear analysis (see e.g. Riecke & Paap 1986).

Finally, it should be noted that the flow oscillations and modulations found between the nonlinear stability boundaries of n_{TG} Taylor–Görtler vortex pairs could be related to the periodicity condition, which considerably restricts the solution space and allows only an even number of Taylor–Görtler vortices. Other methods of investigation must be developed for the computation of long-wavelength effects when infinite systems are to be simulated. A mere extension to larger span aspect ratios is prohibited due to the high numerical cost associated with the increased resolution required in the z-direction.

3.4. *Endwall effects*

The presence of rigid endwalls at $z = \pm\Lambda/2$ has a considerable influence on the Taylor–Görtler vortices which are caused by a bulk-flow instability. The endwall effect was demonstrated experimentally in Albensoeder *et al.* (2001) where the onset of Taylor–Görtler vortices in a square cavity with $\Lambda = 6.55$ was measured. For $Re = 850$ we have found that Taylor–Görtler vortices can exist only within a certain distance from the rigid endwalls in a region symmetrically located in the middle of the cavity around $z = 0$ (figure 8a). In the near-wall regions $1 \lesssim |z| < \Lambda/2$ the Taylor–Görtler vortices are suppressed.

To validate this experimental result the flow was simulated for $\Lambda = 6.55$ and $Re = 850$ using rigid boundary conditions at $z = \pm\Lambda/2$. Within the definition of $\epsilon_s < 10^{-7}$ the numerical solution is steady. For a visual comparison iso-surfaces of the absolute value $|\omega_x|$ of the x-component of the vorticity are shown in figure 8(b). The numerical result is in qualitative agreement with the experimental one. We conclude that a minute leakage of liquid from the cavity to the surrounding liquid bath near the cavity endwalls, which cannot be completely avoided in the experiment, is not responsible for the suppression of the Taylor-Görtler vortices. Hence, an

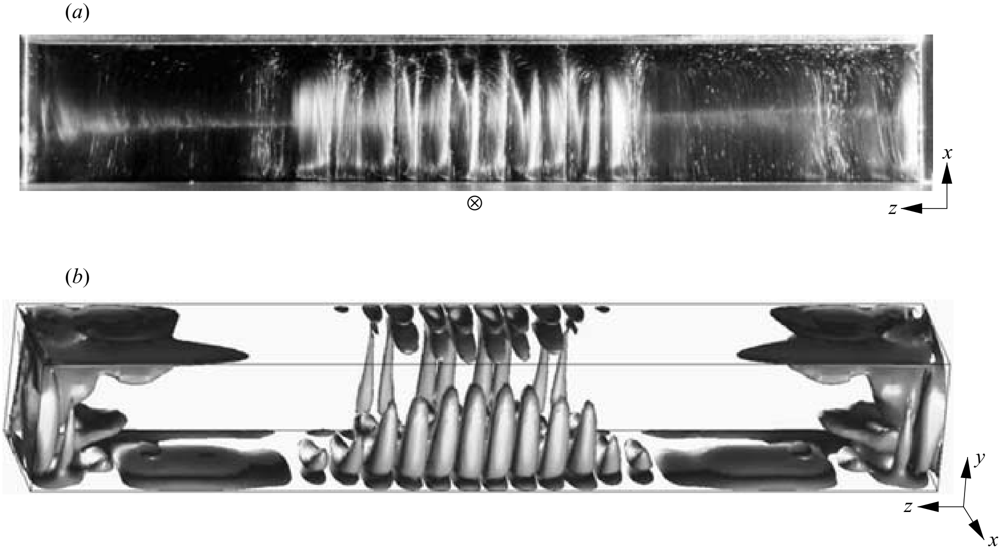

FIGURE 8. (a) Stationary Taylor–Görtler vortices for $\Lambda = 6.55$ and $Re = 850$ reproduced from Albensoeder *et al.* (2001). The flow was visualized by aluminium flitters and illuminated in the plane $y \approx -1/2$ by a light sheet with a thickness of approximately 10 % of the cavity height. The flow is from the top to the bottom where the fluid is accelerated by the moving wall. (b) Numerical simulation of the flow for the same parameters as in (a). Shown are vorticity iso-surfaces $|\omega_x| = 210$. The resolution is $N_x \times N_y \times N_z = 30 \times 30 \times 300$.

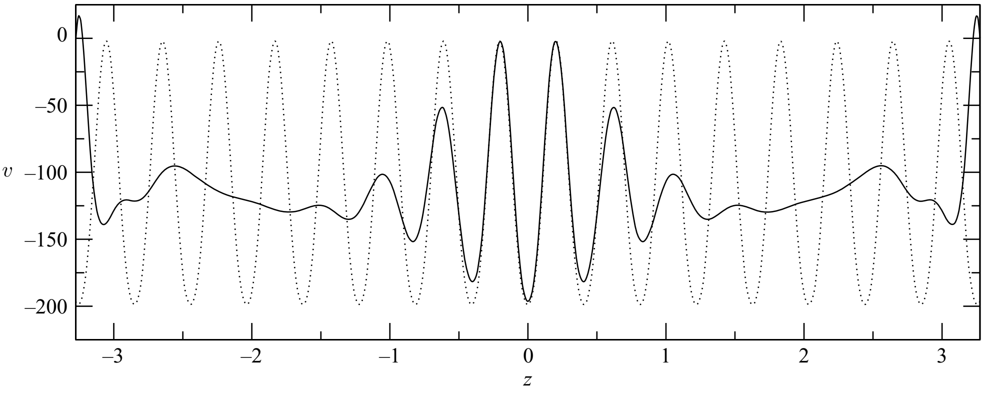

FIGURE 9. Velocity $v(0.263, -0.337, z)$ for rigid (solid line) and periodic (dotted line) boundary conditions as function of the coordinate z for $Re = 850$. The aspect ratios and resolutions are ($\Lambda = 6.55$, $N_x \times N_y \times N_z = 30 \times 30 \times 300$) for rigid boundary conditions and ($\Lambda = 0.407$, $N_x \times N_y \times N_z = 34 \times 34 \times 25$) for periodic boundary conditions.

explanation in terms of a reduced centrifugal effect in the vicinity of both endwalls (see Albensoeder *et al.* 2001) is likely. To provide quantitative data, we show in figure 9 the velocity component v as a function of z along the line $(x, y) = (0.263, -0.337)$ for rigid and periodic boundary conditions.

This explanation is also supported by the results obtained by a variation of the Reynolds number at a constant aspect ratio. When the Reynolds number is reduced quasi-statically the Taylor–Görtler vortices break down at $Re = 835 \pm 5$. This critical Reynolds number is close to the experimentally determined critical Reynolds number $Re_c^{\exp}(\Lambda = 6.55) = 810 \pm 15$ measured by Albensoeder *et al.* (2001) and is only about 6 % larger than the critical Reynolds number for the infinite system (periodic boundary conditions). If, on the other hand, the span aspect ratio is reduced quasi-statically for a constant Reynolds number of $Re = 850$ the Taylor–Görtler vortices vanish at $\Lambda_c(Re = 850) = 6.1 \pm 0.1$. The early breakdown confirms the sensitivity of the onset of Taylor–Görtler vortices to the aspect ratio for rigid endwall boundary conditions.

These numerical results for rigid boundary conditions confirm our previous experimental findings (Albensoeder *et al.* 2001) and extend other investigations, most of which have been carried out for $\Lambda \leqslant 3$ (see e.g. Koseff *et al.* (1983); Koseff & Street (1984*a*, *b*); Prasad & Koseff (1989); and others).

3.5. *Comparison with Taylor vortices*

Taylor–Görtler vortices in the square cavity are similar to Taylor vortices in the Taylor–Couette system when the outer cylinder is at rest (see e.g. DiPrima & Swinney 1985). In the cavity the basic two-dimensional flow consist of a primary vortex in nearly solid-body rotation with its centre at $(x, y) \approx 0$. In the Taylor–Couette system the inner rotating cylinder plays the role of the vortex in solid-body rotation.

To estimate the equivalent radius R_1 and the rotation rate Ω_1 of the primary vortex in the cavity the region of constant vorticity ω_0 on the centrelines $x = 0$ and $y = 0$ of the two-dimensional basic flow has been determined at critical conditions. We obtain $R_1 \approx 0.27$ and $\Omega_1 \approx \omega_0(r = 0)/2 \approx 825$. The radius of the fictitious outer cylinder can be approximated by the wall and the streamline separating the primary vortex from the secondary vortices. Along the separating streamline the velocity $\boldsymbol{u}_0$ is negligibly small; and it vanishes on the rigid walls, which corresponds to stationary boundary conditions $R_2\Omega_2 \approx 0$.

For a comparison of the critical conditions in the cavity with those in circular Couette flow the critical Reynolds number and the critical wavenumber are non-dimensionalized by the scales typically used for the Taylor–Couette system, namely the gap width $\tilde{d} = R_2 - R_1 = 0.23$ and the velocity of the inner cylinder $R_1\Omega_1 \approx 223$. Taking into account that these length and velocity scales are in units of d and ν/d, respectively, we obtain the equivalent critical Reynolds number and wavenumber (superscript TC)

$$Re_c^{\mathrm{TC}} = R_1\Omega_1\tilde{d} \approx 51 \qquad \text{and} \qquad k_c^{\mathrm{TC}} = k_c\tilde{d} \approx 3.5, \tag{3.9}$$

where $k_c = 15.43$ is used (table 1). The equivalent radius ratio for the cavity flow is $\eta = R_1/R_2 = 0.54$.

These values are to be compared with the critical data for the onset of Taylor vortices. For $\eta = 0.55$ DiPrima, Eagles & Ng (1984) obtained $Re_c^{\mathrm{TC}} = 69.5$ and $k_c^{\mathrm{TC}} = 3.155$. The cavity data are of the same order of magnitude and deviate by about 30 % and less than 10 %, respectively, from the critical data in the 'Taylor–Couette system. This qualitative comparison justifies the notion of 'Taylor–Görtler vortices' for the cavity vortices and underlines the centrifugal character of the instability mechanism as proposed by Albensoeder *et al.* (2001).

4. Conclusions

The three-dimensional flow in the one-sided lid-driven square cavity has been investigated by numerical simulations based on a Chebyshev collocation method. The accuracy of the numerical calculations was significantly improved by incorporating local asymptotic solutions in analytical form for the flow in the vicinity of the singular corners. Various flows have been computed for parameters near and above the critical point, including both periodic and rigid boundary conditions in the z-direction.

We found that the bifurcation is supercritical for periodic boundary conditions corresponding to the critical wavelength $\Lambda = \lambda_c$. By comparing the numerically calculated time-asymptotic solutions with the steady-state solutions of a fifth-order amplitude equation it was shown that the amplitude for $\Lambda = \lambda_c$ scales like $\varepsilon^{1/2}$ only in the narrow range $\varepsilon \ll 1/400$. On typical scales, however, the amplitude of the three-dimensional flow grows like $\varepsilon^{1/4}$. This behaviour can be understood if one takes into account the dependence of the bifurcation on the period Λ: the flow for $\Lambda \lesssim \lambda_c$ bifurcates supercritically, whereas it bifurcates subcritically for $\Lambda \gtrsim \lambda_c$.

Calculations for periodic boundary conditions and periods much larger then the critical wavelength have shown that the stable band of wavenumbers is significantly reduced if ε is large, an effect which is expected from the Eckhaus instability. For $\varepsilon \to 0$, however, the linearly unstable band is also recovered for the largest values of Λ considered.

Computations carried out for rigid endwall conditions confirmed the experimental results of Albensoeder *et al.* (2001). Rigid endwalls suppress Taylor–Görtler vortices within a certain distance from the walls. Hence, Taylor–Görtler vortices in the driven cavity can only be observed for sufficiently large span aspect ratios Λ.

This work has been supported by Deutsche Forschungsgemeinschaft under grant numbers Ku896/5-2 and Ku896/8-1. All computations were performed at the Center of Applied Space Technology and Microgravity (ZARM) of the University of Bremen.

REFERENCES

Albensoeder, S. 2004 *Lineare und nichtlineare Stabilität inkompressibler Strömungen im zweiseitig angetriebenen Rechteckbehälter*. Cuvillier Verlag.

Albensoeder, S. & Kuhlmann, H. C. 2005 Accurate three-dimensional lid-driven cavity flow. *J. Comput. Phys.* **206**, 536–558.

Albensoeder, S., Kuhlmann, H. C. & Rath, H. J. 2001 Three-dimensional centrifugal-flow instabilities in the lid-driven cavity problem. *Phys. Fluids* **13**, 121–135.

Botella, O. 1998 Résolution numérique de problèmes de Navier–Stokes singuliers par une méthode de projection Tchebychev. PhD thesis, Université de Nice–Sophia Antipolis.

Botella, O. & Peyret, R. 1998 Benchmark spectral results on the lid-driven cavity flow. *Computers Fluids* **27**, 421–433.

Burggraf, O. R. 1966 Analytical and numerical studies of the structure of steady separated flows. *J. Fluid Mech.* **24**, 113–151.

Chiang, T. P., Hwang, R. R. & Sheu, W. H. 1997 On endwall corner vortices in a lid-driven cavity. *Trans. ASME: J. Fluids Engng* **119**, 201–214.

Cross, M. C. & Hohenberg, P. C. 1993 Pattern formation outside of equilibrium. *Rev. Mod. Phys.* **65**, 851–1112.

Deville, M., Lê, T.-H. & Morchoisne, Y. 1992 *Numerical Simulation of 3-D Incompressible Unsteady Viscous Laminar Flows*. Notes on Numerical Fluid Mechanics, vol. 36. Braunschweig: Vieweg.

Ding, Y. & Kawahara, M. 1998 Linear stability of incompressible fluid flow in a cavity using finite element method. *Intl J. Num. Meth. Fluids* **27**, 139–157.

Ding, Y. & Kawahara, M. 1999 Three-dimensional linear stability analysis of incompressible viscous flows using the finite element method. *Intl J. Num. Meth. Fluids* **31**, 451–479.

DiPrima, R. C., Eagles, P. M. & Ng, B. S. 1984 The effect of radius ratio on the stability of Couette flow and Taylor vortex flow. *Phys. Fluids* **27**, 2403–2411.

DiPrima, R. C. & Swinney, H. L. 1985 Instabilities and transition in flow between concentric rotating cylinders. In *Hydrodynamic Instabilities and the Transition to Turbulence* (ed. H. L. Swinney & J. P. Gollub). Topics in Applied Physics, vol. 45, pp. 139–180. Springer.

Drazin, P. G. & Reid, W. H. 1981 *Hydrodynamic Stability*. Cambridge University Press.

Eckhaus, W. 1965 *Studies in Nonlinear Stability*. Springer.

Fauve, S. 1998 *Pattern Forming Instabilities*, chap. 4, pp. 387–491. Cambridge University Press.

Goodrich, J. W., Gustafson, K. & Halasi, K. 1990 Hopf bifurcation in the driven cavity. *J. Comput. Phys.* **90**, 219–261.

Guermond, J.-L., Migeon, C., Pineau, G. & Quartapelle, L. 2002 Start-up flows in a three-dimensional rectangular driven cavity of aspect ratio 1:1:2 at $Re = 1000$. *J. Fluid Mech.* **450**, 169–199.

Gupta, M. M., Manohar, R. P. & Noble, B. 1981 Nature of viscous flows near sharp corners. *Computers Fluids* **9**, 379–388.

Haidvogel, D. B. & Zang, T. 1979 The accurate solution of Poisson's equation by expansion in Chebyshev polynomials. *J. Comput. Phys.* **30**, 167–180.

Haldenwang, P., Labrosse, G., Abboudi, S. & Deville, M. 1984 Chebyshev 3-D spectral and 2-D pseudospectral solvers for the Helmholtz equation. *J. Comput. Phys.* **55**, 115–128.

Hancock, C., Lewis, E. & Moffatt, H. K. 1981 Effects of inertia in forced corner flows. *J. Fluid Mech.* **112**, 315–327.

Heinrichs, W. 1998 Splitting techniques for the unsteady Stokes equations. *SIAM J. Num. Anal.* **35**, 1646–1662.

Koseff, J. R. & Street, R. L. 1984*a* On endwall effects in a lid-driven cavity flow. *Trans. ASME: J. Fluids Engng* **106**, 385–389.

Koseff, J. R. & Street, R. L. 1984*b* Visualization studies of a shear driven three-dimensional recirculating flow. *Trans. ASME: J. Fluids Engng* **106**, 21–29.

Koseff, J. R., Street, R. L., Gresho, P. M., Upson, C. D., Humphrey, J. A. C. & To, W.-M. 1983 A three-dimensional lid-driven cavity flow: Experiment and simulation. In *Proc. 3rd Intl Conf. on Numerical Methods in Laminar and Turbulent Flow* (ed. C. Taylor), pp. 564–581. Pineridge Press.

Ku, H. C., Hirsh, R. S. & Taylor, T. D. 1987 A pseudospectral method for solution of the three-dimensional incompressible Navier–Stokes equations. *J. Comput. Phys.* **70**, 439–462.

Moffatt, H. K. 1964 Viscous and resistive eddies near a sharp corner. *J. Fluid Mech.* **18**, 1–18.

Newell, A. C. & Whitehead, J. A. 1969 Finite bandwidth, finite amplitude convection. *J. Fluid Mech.* **38**, 279.

Pan, F. & Acrivos, A. 1967 Steady flows in rectangular cavities. *J. Fluid Mech.* **28**, 643–655.

Peyret, R. 2002 *Spectral Methods for Incompressible Viscous Flow*. Applied Mathematical Sciences, vol. 148. Springer.

Poliashenko, M. & Aidun, C. K. 1995 A direct method for computation of simple bifurcations. *J. Comput. Phys.* **121**, 246–260.

Prasad, A. K. & Koseff, J. R. 1989 Reynolds number and endwall effects on a lid-driven cavity flow. *Phys. Fluids* A **1**, 208–218.

Rhee, H. S., Koseff, J. R. & Street, R. L. 1984 Flow visualization of recirculating flow by rheoscopic liquid and liquid crystal technique. *Exps. Fluids* **2**, 57–64.

Riecke, H. & Paap, H.-G. 1986 Stability and wave-vector restriction of axisymmetric Taylor vortex flow. *Phys. Rev.* A **33**, 547–553.

Schreiber, R. & Keller, H. B. 1983 Driven cavity flows by efficient numerical techniques. *J. Comput. Phys.* **49**, 310–333.

Shankar, P. N. & Deshpande, M. D. 2000 Fluid mechanics in the driven cavity. *Annu. Rev. Fluid Mech.* **32**, 93–136.

Shatrov, V., Mutschke, G. & Gerbeth, G. 2003 Three-dimensional linear stability analysis of lid-driven magnetohydrodynamic cavity flow. *Phys. Fluids* **15**, 2141–2151.

Sipp, D. & Jacquin, L. 2000 Three-dimensional centrifugal-type instabilities of two-dimensional flows in rotating systems. *Phys. Fluids* **12**, 1740–1748.

Spasov, Y., Herrero, J., Grau, F. X. & Giralt, F. 2003 Linear stability analysis and numerical calculations of the lid-driven flow in a toroidally shaped cavity. *Phys. Fluids* **15**, 134–146.

Theofilis, V. 2000 Globally unstable basic flows in open cavities. *AIAA Paper* 2000-1965.

Theofilis, V., Duck, P. W. & Owen, J. 2004 Viscous linear stability analysis of rectangular duct and cavity flows. *J. Fluid Mech.* **505**, 249–286.

Triantafillopoulos, N. G. & Aidun, C. K. 1990 Relationship between flow instability in short-dwell ponds and cross directional coat weight nonuniformities. *TAPPI J.* **73**, 127–136.

de Vahl Davis, G. & Mallinson, G. D. 1976 An evaluation of upwind and central difference approximations by a study of recirculating flow. *Computers Fluids* **4**, 29–43.